



## 2D ZnO mesoporous single-crystal nanosheets with exposed {0001} polar facets for the depollution of cationic dye molecules by highly selective adsorption and photocatalytic decomposition

Jing Liu<sup>a,1</sup>, Zhi-Yi Hu<sup>b,1</sup>, Yao Peng<sup>a</sup>, Hua-Wen Huang<sup>a</sup>, Yu Li<sup>a,\*</sup>, Min Wu<sup>a</sup>, Xiao-Xing Ke<sup>b</sup>, Gustaaf Van Tendeloo<sup>b</sup>, Bao-Lian Su<sup>a,c,d,\*</sup>

<sup>a</sup> Laboratory of Living Materials at State Key Laboratory of Advanced Technology for Materials Synthesis and Processing, Wuhan University of Technology, 122 Luoshui Road, 430070 Wuhan, China

<sup>b</sup> EMAT (Electron Microscopy for Materials Science), University of Antwerp, 171 Groenenborgerlaan, B-2020 Antwerp, Belgium

<sup>c</sup> Laboratory of Inorganic Materials Chemistry (CMI), University of Namur, 61 rue de Bruxelles, B-5000 Namur, Belgium

<sup>d</sup> Department of Chemistry and Clare Hall, University of Cambridge, Lensfield Road, Cambridge CB2 1EW, United Kingdom

### ARTICLE INFO

#### Article history:

Received 14 May 2015

Received in revised form 28 July 2015

Accepted 29 July 2015

Available online 1 August 2015

#### Keywords:

2D ZnO mesoporous single-crystal nanosheets

Polar facets

Photocatalytic activity and selectivity

Organic molecules

Colloidal templating approach

### ABSTRACT

Two dimensional (2D) ZnO nanosheets are ideal system for dimensionally confined transport phenomenon investigation owing to specific surface atomic configuration. Therefore, 2D ZnO porous nanosheets with single-crystal nature and {0001} polar facets, likely display some specific physicochemical properties. In this work, for the first time, 2D ZnO mesoporous single-crystal nanosheets (ZnO-MSN) with {0001} polar facets have been designed and prepared via an intriguing colloidal templating approach through controlling the infiltration speed for the suspension of EG-capped ZnO nanoparticles and polymer colloids. The EG-capped ZnO nanoparticles are very helpful for single-crystal nanosheet formation, while the polymer colloids play dual roles on the mesoporosity generation and {0001} polar facets formation within the mesopores. Such special 2D structure not only accelerates the hole-electron separation and the electron transportation owing to the single-crystal nature, but also enhances the selective adsorption of organic molecules owing to the porous structure and the exposed {0001} polar facets with more O-termination (000-1) surfaces: the 2D ZnO-MSN shows highly selective adsorption and significantly higher photodegradation for positively charged rhodamine B than those for negatively charged methyl orange and neutral phenol, comparing with ZnO nanoparticles (ZnO-NP) and ZnO commercial nanoparticles (ZnO-CNP) with high surface areas. This work may shed some light on better understanding the synthesis of 2D porous single-crystal nanosheet with exposed polar surfaces and photocatalytic mechanism of nanostructured semiconductors in a mixed organic molecules system.

© 2015 Elsevier B.V. All rights reserved.

### 1. Introduction

Zinc oxide (ZnO) has been widely studied in environmental and energy-related applications, such as photocatalysis, solar cell devices, sensors and catalyst supports. To date, many reports have been published on synthesizing various ZnO nanostructures, such as nanorods, nanowires, nanosheets, core-shell structures and

porous structures [1–4]. For photocatalysis, previous reports have demonstrated that the morphologies of the ZnO nanostructures can greatly affect their effective surface areas, their interaction with organic molecules, their photodegradation capability of organic molecules, and consequently the whole photocatalytic activities [5–8].

Among the various nanostructures, two dimensional (2D) ZnO nanostructures, due to their high anisotropy and nanometer-scale thickness, possess outstanding properties, and therefore have recently aroused extensive attention [6,9–11]. This unique morphology generates very specific surface atomic configuration and high exposure degree of active crystal facets, leading to new physicochemical properties such as enhanced adsorption capability and catalytic selectivity [12,13]. On the other hand, 2D nanostructures are considered as ideal system for dimensionally confined transport

\* Corresponding authors at: Laboratory of Living Materials at State Key Laboratory of Advanced Technology for Materials Synthesis and Processing, Wuhan University of Technology, 122 Luoshui Road, 430070 Wuhan, China.

E-mail addresses: [yu.li@whut.edu.cn](mailto:yu.li@whut.edu.cn) (Y. Li), [baoliansu@whut.edu.cn](mailto:baoliansu@whut.edu.cn), [bao-lian.su@unamur.be](mailto:bao-lian.su@unamur.be), [bls26@cam.ac.uk](mailto:bls26@cam.ac.uk) (B.-L. Su).

<sup>1</sup> These two authors contributed equally to this work.

phenomenon investigation due to electron collection improvement [14]. In particular, 2D nanosheet with single-crystal nature results in photogenerated charges smoothly walking through the structure and thus accelerating the charges transport [15]. As photocatalytic reaction occurs at the interface between catalysts and organic molecules, the specific surface atomic configuration and {0001} polar facets of ZnO strongly influence its photocatalytic activity [16]. In addition, fine-tuning of the surface orientation and/or the {0001} polar facets leads to the highly enhanced photocatalytic activity of ZnO nanostructures [6,13,15]. Thus, it is conceivable that 2D ZnO single-crystal nanosheet with porous structure and exposed {0001} polar facets is likely a promising demonstration for largely photocatalytic properties enhancement because this special structure can not only be beneficial for the hole-electron separation and the electron transportation, but also enhance the selective adsorption and photodegradation of organic molecules.

So far, conventional method on synthesizing ZnO nanosheet structure with {0001} polar facets is physical method. For example, Tusche et al. have reported pulsed laser deposition for thick ZnO (0001) films on Ag (111) [14]. However, this method is not easy to introduce porosity in 2D nanosheet structure. As a widely accepted facile wet-chemistry approach, hydrothermal method has been used to get the porous ZnO nanosheets via calcination of the intermediates from acetate-intercalated zinc hydroxy double salt or hydroxide zinc carbonate [17,18], whereas the resulting porous ZnO nanosheets are polycrystalline [18,19]. Recent reports have demonstrated that ZnO nanosheets with {0001} polar facets can be generated using polymer or surfactants as growth modifiers [20]. The obtained ZnO nanosheets with {0001} polar facets however are generally without porous structure [21]. Most recently, Crossland et al. have reported TiO<sub>2</sub> mesoporous single-crystal powders via a self-assembled SiO<sub>2</sub> colloidal template based on the seeded nucleation [22]. But this method is not easy for 2D nanosheet preparation. Therefore, designing and synthesizing 2D ZnO mesoporous single-crystal nanosheet with exposed {0001} polar facets is still a big challenge via a facile wet-chemistry method.

Herein, on the basis of our previous work on colloidal templating method [23–28], for the first time, we report synthesizing 2D ZnO mesoporous single-crystal nanosheet (ZnO-MSN) with exposed {0001} polar facets via a very intriguing colloidal templating method. Most importantly, such mesoporous single-crystal sheet structure exhibits unprecedentedly adsorption selectivity and photocatalytic activity toward cationic organic molecules compared to anionic and neutral organic molecules. To the best of our knowledge, this is the first time to demonstrate the preferential selective adsorption of organic molecules for ZnO nanostructures.

## 2. Experimental

### 2.1. Materials

Styrene, methyl methacrylate (MMA), sulfo propyl methacrylate potassium (SPMAP), ammonium persulfate, ammonium bicarbonate, Zn(Ac)<sub>2</sub>·2H<sub>2</sub>O, ethylene glycol (EG), rhodamine B (RhB), methyl orange (MO) and phenol were purchased from Aldrich.

### 2.2. Polymer colloidal sphere preparation

The 250 nm monodispersed colloids of poly(styrene-methyl methacrylate-sulfo propyl methacrylate potassium) (abbreviated as P(St-MMA-SPMAP)) beads were synthesized by a soap-free emulsion polymerization: 22.5 mL styrene, 1.25 mL MMA and 110 mL water were heated to 70 °C under N<sub>2</sub> atmosphere. 10 mL water with 0.4 g ammonium persulfate, 0.8 g ammonium bicar-

bonate and 0.3 g SPMAP were added to initiate the polymerization reaction, which was stopped after 8 h.

### 2.3. ZnO-MSN preparation

2D ZnO mesoporous single-crystal nanosheet was synthesized as follows: first, 0.01 mol Zn(Ac)<sub>2</sub>·2H<sub>2</sub>O was dissolved in 20 mL EG at room temperature and then transferred to a Teflon-lined stainless steel autoclave and heated at 160 °C for 1 h. After the mixture was cooled to room temperature, the EG-capped ZnO nanoparticles were obtained and further dispersed in ethanol to form EG-capped ZnO suspension. Then 20 mL P(St-MMA-SPMAP) monodispersed colloids were added into EG-capped ZnO suspension and stirred for 48 h at room temperature. The ZnO/P(St-MMA-SPMAP) composites were slowly filtrated and dried at 40 °C for self-assembling into layered structure. The resulting layered ZnO/P(St-MMA-SPMAP) composites were calcined at 300 °C for 2 h and subsequently raised to 450 °C for 8 h. Finally, 2D ZnO-MSN was obtained after cooling down to room temperature.

### 2.4. ZnO-NP preparation

0.01 mol Zn(Ac)<sub>2</sub>·2H<sub>2</sub>O was dissolved in 20 mL EG at room temperature and then transferred to a Teflon-lined stainless steel autoclave and heated at 160 °C for 1 h to obtain the EG-capped ZnO nanoparticles. Then the EG-capped ZnO nanoparticles were washed by absolute ethanol and water for several times and calcined at 450 °C for 8 h. Finally, ZnO-NP was obtained after cooling down to room temperature.

### 2.5. Characterizations

X-ray diffraction (XRD) patterns were obtained with a Bruker D8 Advanced diffractometer using Cu K $\alpha$  radiation ( $\lambda = 1.54056 \text{ \AA}$ ). Scanning electron microscopy (SEM) was carried out on a Hitachi S-4800 microscope with field emission gun, operated at 5.0 kV. Transmission electron microscopy (TEM) was carried out on a JEOL JEM-3000F, operated at 300 kV. High resolution transmission electron microscopy (HRTEM) was carried out on a FEI Titan 80-300 “cubed” microscope with aberration-correctors for the imaging lens and the probe-forming lens, as well as a monochromator, operated at 300 kV. The Brunauer–Emmett–Teller (BET) specific surface area of the samples was analyzed by nitrogen adsorption in a Micromeritics Tristar II 3020 nitrogen adsorption–desorption apparatus according to the Barret–Joyner–Halenda (BJH) method from the N<sub>2</sub> adsorption isotherms. The absorption spectra were collected with a UV2550 (SHIMADZU) UV–vis spectrometer.

### 2.6. Photocatalytic activity measurements

The photocatalytic activities of the product were investigated using RhB, MO and phenol aqueous solution. The reactor was illuminated under simulated solar light (250–780 nm, PLS-SXE-300UV with an UV light intensity of 34 mW cm<sup>−2</sup> and a visible light intensity of 158 mW cm<sup>−2</sup>, Beijing) with a distance of 30 cm at room temperature. For the single pollutant, the concentration of RhB, MO and phenol was  $\sim 1 \times 10^{-5}$  mol/L, respectively. For the mixed pollutants, the concentration of RhB, MO and phenol was  $0.65 \times 10^{-5}$  mol/L,  $0.7 \times 10^{-5}$  mol/L and  $3.7 \times 10^{-3}$  mol/L, respectively. Experiments were conducted as follows: 100 mg catalysts were added into the reactor containing 100 mL organic pollutant solution. The solution was magnetically stirred in the dark for 1 h to achieve adsorption–desorption equilibrium and then illuminated under simulated solar light. 1 mL solution was taken out and evaluated using UV2550 (SHIMADZU) UV–vis spectrometer at 10 min or 30 min interval. The photocatalytic reaction based on first-order,

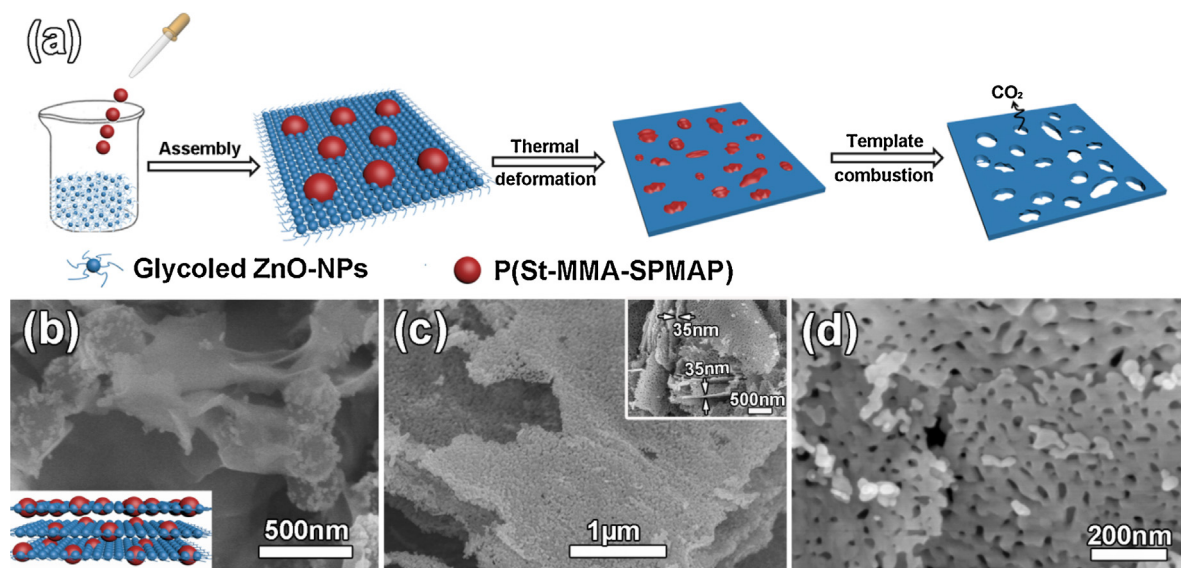


**Fig. 1.** (a) Schematic illustration of the ZnO-MSN synthesis, (b) SEM images of the layer assembled ZnO/P(St-MMA-SPMAP) composites with the inset showing the perspective view of schematic image, (c) low magnification SEM image with the inset showing the thickness of ZnO-MSN and (d) high magnification SEM image of ZnO-MSN.

$\ln(C_0/C) = kt$ , where  $C_0$  and  $C$  are the initial and actual pollutant concentration, respectively, and  $k$  is the apparent rate constant of the degradation.

### 3. Results and discussion

The well dispersed and single polymeric colloids (250 nm in size, Fig. S1) were used as template to create mesoporosity in ZnO single-crystal nanosheets. Fig. 1a illustrates the schematic synthesis strategy. The polymer colloids were dispersed in the EG-capped ZnO nanoparticles (a typical SEM image shown in Fig. S2) to form a ZnO/colloids suspension, which was slowly filtrated to get a layer of assembled ZnO/colloidal composites (Fig. 1b). During the combustion process, the polymer colloids tend to soften and deform to small fragments. After the totally combustion of the small fragments, the mesoporous nanosheets are obtained (Fig. 1a). It is noted that the infiltration rate controlling is very important for 2D ZnO-MSN formation. Without controlling the infiltration rate, the ZnO/colloids tend to self-assemble into hierarchically macro-mesoporous structure (Fig. S3). The EG-capped ZnO nanoparticles can affect the interaction between the ZnO nanoparticles and colloidal spheres, and are helpful for nanosheet formation during the calcination process. Without polymer colloids, only ~30 nm irregular ZnO nanoparticles can be obtained (Fig. S4a). As ZnO nanostructures easily grow along the {0001} polar facets [3,29–32], the inserted colloidal spheres then not only offer the porous structure, but also direct the aggregation of EG-capped ZnO nanoparticles, leading to the exposure of {0001} polar facets within the formed mesopores during the colloidal template combustion (Fig. 1a).

Fig. 1c presents an overview of ZnO-MSN over a large area, indicating a high yield and uniformity of the structure. Fig. 1c inset reveals the thickness of ZnO-MSN of ~35 nm (the enlargement of the inset shown in Fig. S5). Fig. 1d gives a high magnification SEM image, displaying interconnected pore network with a uniform pore size in the range of 20–50 nm. The XRD patterns collected from the product (Fig. 2a) show a high crystallinity of the as-synthesized porous nanosheet. All diffraction peaks match well with the hexagonal wurtzite-structured ZnO (JCPDS No. 079-2205). The mesoporous structure is further confirmed by the nitrogen adsorption–desorption isotherm (Fig. 2b), which gives a specific

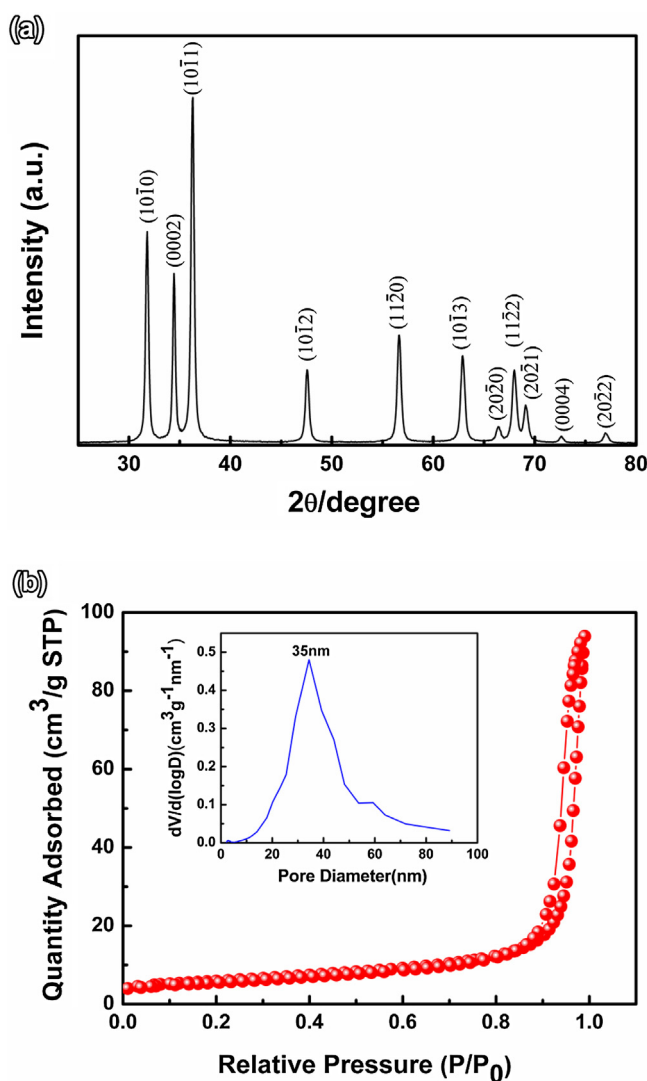


**Fig. 2.** (a) The XRD pattern and (b) nitrogen adsorption–desorption isotherm and the pore distribution (inset) of ZnO-MSN.



**Table 1**

The structure parameters and zeta potential results of ZnO-MSN, ZnO-NP and ZnO-CNP.

Samples	ZnO-MSN	ZnO-NP	ZnO-NP	H <sub>2</sub> O
BET surface area (m <sup>2</sup> g <sup>-1</sup> )	20	42	38	N/A
Pore size (nm)	35	12	21	N/A
Band gap (eV)	3.02	3.0	2.94	N/A
Average potential (mV)	5.1 ± 0.5	5.2 ± 0.5	15 ± 0.5	3.1

BET surface area of 20 m<sup>2</sup> g<sup>-1</sup> and the average pore size of 35 nm (Fig. 2b inset and Table 1), being in very good agreement with the SEM observations (Fig. 1c and d).

The TEM images further reveal the porous feature and the single-crystal nature of ZnO-MSN, confirming a pore-size ranging from 20 nm to 50 nm (Fig. 3). Our intensive TEM observations demonstrate that nearly all flat-lying nanosheets are orientated along either [10–10] or [–12–10] zone axis. To make sure of the single-crystal nature of the nanosheets, we conducted intensive selected area electron diffraction (SAED) patterns upon randomly selecting the areas from different nanosheets using the largest selected-area aperture available (Fig. 3a and d upper inset and Fig. S6). All the SAED patterns show no continuous diffraction rings or many other diffraction spots along other zone axes upon our intensive observations, confirming the single-crystal nature of the nanosheets. Representative images are shown in Fig. 3a and d, respectively. Cor-

responding orientations of the nanosheets are respectively [10–10] (Fig. 3a upper inset) and [–12–10] (Fig. 3d upper inset). This can be explained from the ZnO single-crystals growth [1,3,29–31]. Because the {–12–10} and {10–10} facets are non-polar surfaces and have lower surface energies than the polar surface formed by positive charged Zn-(0001) (Zn terminated) surface and negative charged O-(000 $\bar{1}$ ) (O-terminated) surface, the {–12–10} and {10–10} facets are, in general, largely exposed due to their low surface energies (Fig. 3b–c and e–f). EG-capped ZnO nanoparticles nucleation and colloidal spheres calcination however, lead to the mesopores formation and the exposure of {0001} polar facets within mesopores, as schematically presented in Figs. 1 a and 3 b and e. It is thus the colloidal spheres leading to the generation of mesopores and exposed {0001} polar facets.

A close and detailed observation of ZnO-MSN was carried out to confirm the (0001) polar surface in the porous single-crystal nanosheet structure. Fig. 4a demonstrates a full-scale HRTEM image of one nanosheet. The atomic resolution image in zone 1 clearly demonstrates a (0001) polar surface. The sharp edge of the pore is free of amorphous contamination (Fig. 4b). Although some contrast changes can be observed in zone 2 (Fig. 4c), the HRTEM image still reveal the perfect ZnO crystal lattices without obvious dislocations. We presume this situation is mainly caused by the different thickness from the nanosheet. Similar to zone 2, the whole area of zone 3 is still a single-crystal without any apparent defects (Fig. 4d). At

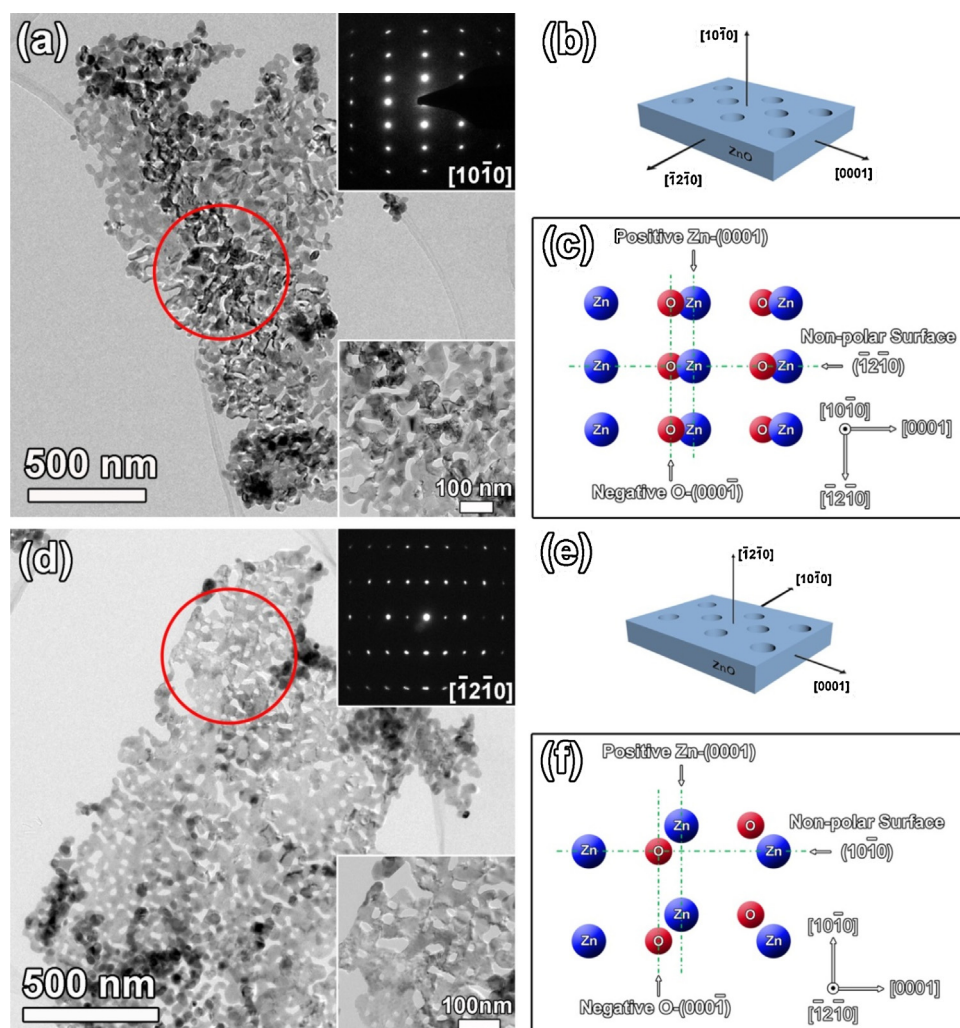


**Fig. 3.** (a) and (d) low magnification TEM images and their corresponding enlargement of the indicated areas (lower inset) and selected area electron diffraction (SAED) (upper inset), (b) and (e) two schematic models of ZnO-MSN along (0001) direction, (c) and (f) models of atomic columns along [10–10] and [–12–10] zone axes, respectively.

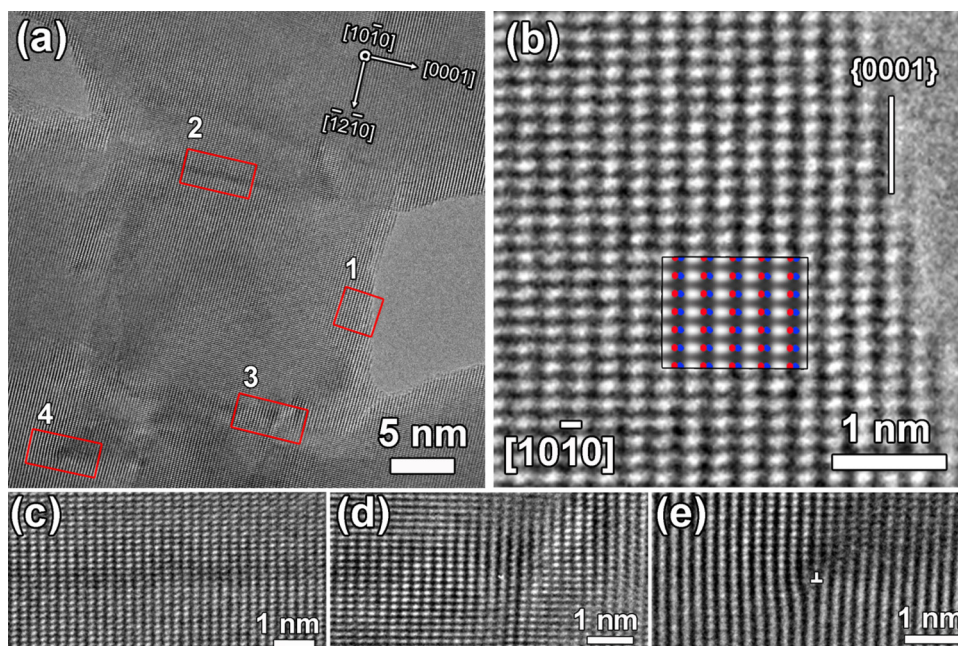


**Fig. 4.** (a) A wide view of HRTEM image for one mesopore, (b) atomic resolution TEM image indicated in (a) with zone 1 red box and simulated image (the inset): Zn columns (blue) and O columns (red), (c–e) corresponding magnified atomic resolution TEM images indicated in (a) with red boxes (c: zone 2, d: zone 3, e: zone 4). (For interpretation of the references to color in text and figure legend, the reader is referred to the web version of this article.)

zone 4, a typical edge dislocation is observed (Fig. 4e). This defect still insists the single-crystal nature of the nanosheet, although not being a perfect single-crystal with an undulant and distorted surface plane. Therefore, according to our intensive TEM observations, the contrast changes are mostly caused by the thickness and distortion of crystals. And the other parts are caused by the dislocations (like edge dislocation). The HRTEM simulation along  $[10\bar{1}0]$  using the multi-slice method [33] is shown in Fig. 4b as inset, and the positions of Zn (blue) and O (red) columns are indicated. The polar termination on the exposed facets induced by the presence of the pores is therefore unambiguously determined. However, it is hard to determine the positively charged Zn-(0001) (Zn terminated) surface or negatively charged O-(000 $\bar{1}$ ) (O-terminated) surface from the HRTEM observations.

It is found that different crystalline orientations possess different electronic, optical and acoustic properties [15], and previous reports suggested that the polar facets with positive Zn-(0001) or negative O-(000 $\bar{1}$ ) surface lead to a significantly photocatalytic activity enhancement on single organic pollutant molecules [6]. The photocatalytic performance of ZnO with exposed {0001} polar facets for different charged organic molecules has seldom reported so far. Investigating the photocatalytic performance of ZnO-MSN for different charged molecules is likely not only a promising approach to better understand the photocatalytic reaction mechanism of ZnO-MSN with exposed {0001} polar facets but also more closely to the reality of polluted water. Furthermore, it is possible to distinguish the photodegradation sequence of differently charged molecules and Zn or O termination of the exposed {0001} polar facets through the interaction between ZnO and organic molecules.

Three differently charged organic model molecules, cationic rhodamine B (RhB), anionic methyl orange (MO) and neutral phenol have been used. The experiments were firstly performed using RhB, MO and phenol, respectively. Then a mixture of these organic molecules was used to study the effect of exposed {0001} polar facets on the photocatalytic activity and the selectivity of ZnO-MSN towards these model molecules.

The photocatalyst has been immersed in dark for 1 h in aqueous solution containing single or mixed pollutant molecules to study their adsorption behaviors (left region in Fig. 5a and b). It is evidenced that in both cases, single or mixed pollutant molecules, the adsorption capacity of ZnO-MSN towards cationic RhB is much higher than those towards neutral phenol and anionic MO. In the presence of single pollutant molecules, the adsorption capacity of ZnO-MSN towards organic molecules varies from 23.2% RhB to 16.9% phenol and to 7.1% MO. In the mixed pollutant molecules solution, there is an adsorption competition among the differently charged molecules. It is interesting to note that the same trend is observed with a much higher adsorption capacity towards RhB (18.8%) compared to phenol (10.7%) and MO (1.6%) due to the preferential adsorption for cationic RhB. This indicates that ZnO-MSN presents higher adsorption selectivity toward RhB than MO and phenol. The adsorption of MO on ZnO-MSN is much less favorable. This analysis implies that ZnO-MSN contains more negatively charged O-terminated (000 $\bar{1}$ ) surfaces, generating more coulombic attraction with positively charged RhB.

Under simulated solar light illumination, the photodegradation of organic molecules occurs. The progressive spectral changes of the photodegradation of the single and mixed pollutant molecules over ZnO-MSN are presented in Fig. S7. The characteristic absorption peaks of the three organic pollutant molecules are clearly displayed, indicating no interaction between the molecules in the mixture. It is clear that the photodegradation of RhB is the quickest (Fig. 5a and b). In the single pollutant molecules solution, the degradation rates for RhB, MO and phenol are  $5.8 \times 10^{-2}$ ,  $4.1 \times 10^{-2}$  and  $1.7 \times 10^{-2}$ , respectively. In the mixed pollutant molecules solution, the degradation rate changes from  $2.0 \times 10^{-2}$  for RhB,  $0.94 \times 10^{-2}$  for MO to  $0.68 \times 10^{-2}$  for phenol due to the competition effect. Compared to the presence of single pollutant molecules, the degradation rate of cationic RhB in the mixture is much higher than those of anionic MO and neutral phenol. These results demonstrate that the ZnO-MSN has the highest selective adsorption and the highest photodegradation activity toward RhB. It is worth noting that although the adsorption of neutral phenol is higher than that of anionic MO, both

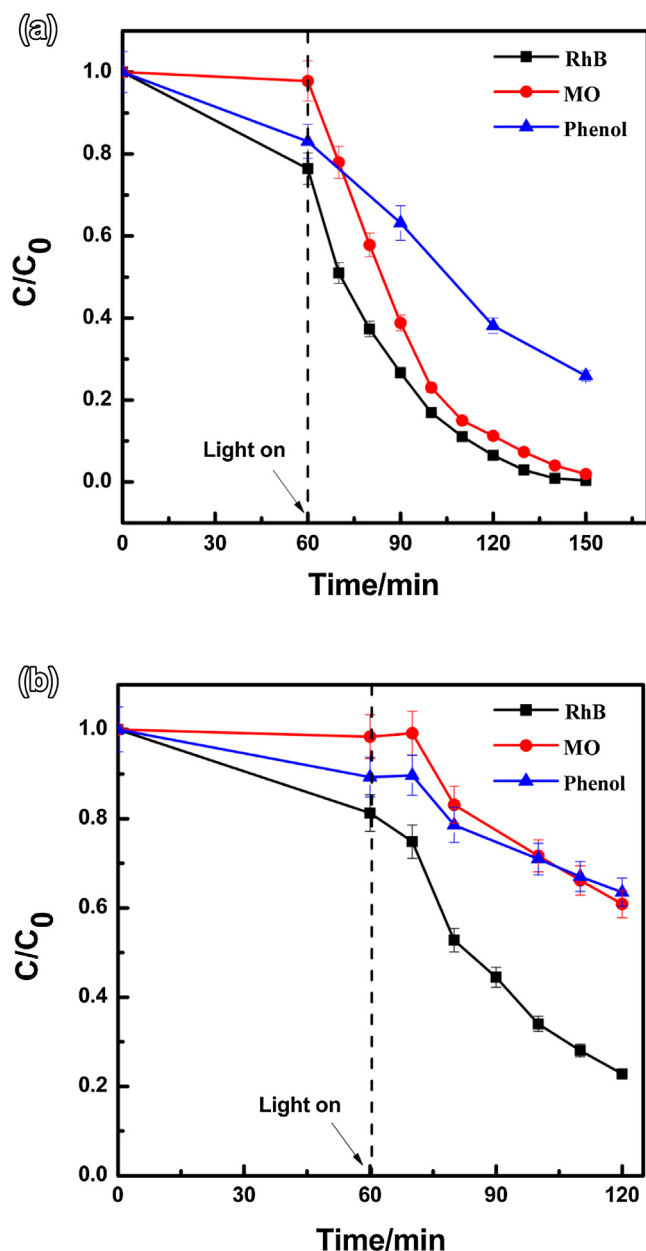


Fig. 5. (a) Comparison of photocatalytic decomposition of single pollutant and (b) mixed molecules on ZnO-MSN.

the photodegradation rates of phenol in single and mixed pollutant molecules are slower than those of MO. This can be explained as MO is a typical azo molecular stuff with conjugated benzene group, being easily damaged by the photogenerated charges comparing to the quite stable single benzene ring within phenol [34].

In order to further investigate the adsorption selectivity of ZnO-MSN and prove the effect of polar facets and single-crystal nature on the photocatalytic efficiency,  $\sim 30$  nm ZnO-NP with specific BET surface area of  $42 \text{ m}^2 \text{ g}^{-1}$  (Fig. S4) and  $\sim 30$  nm irregular ZnO commercial nanoparticles (ZnO-CNP) with specific BET surface area of  $38 \text{ m}^2 \text{ g}^{-1}$  (Fig. S8) were used in this experiment. Table 1 presents the structure parameters in detail. The progressive spectral changes of the photodegradation of mixed pollutant molecules over ZnO-CNP and ZnO-NP are presented in Figs. S9 and S10. To exclude the surface area effect, surface normalized adsorption of these different molecules is conducted on ZnO-MSN, ZnO-NP and ZnO-CNP (Fig. 6a). All the samples demonstrate no obvious difference

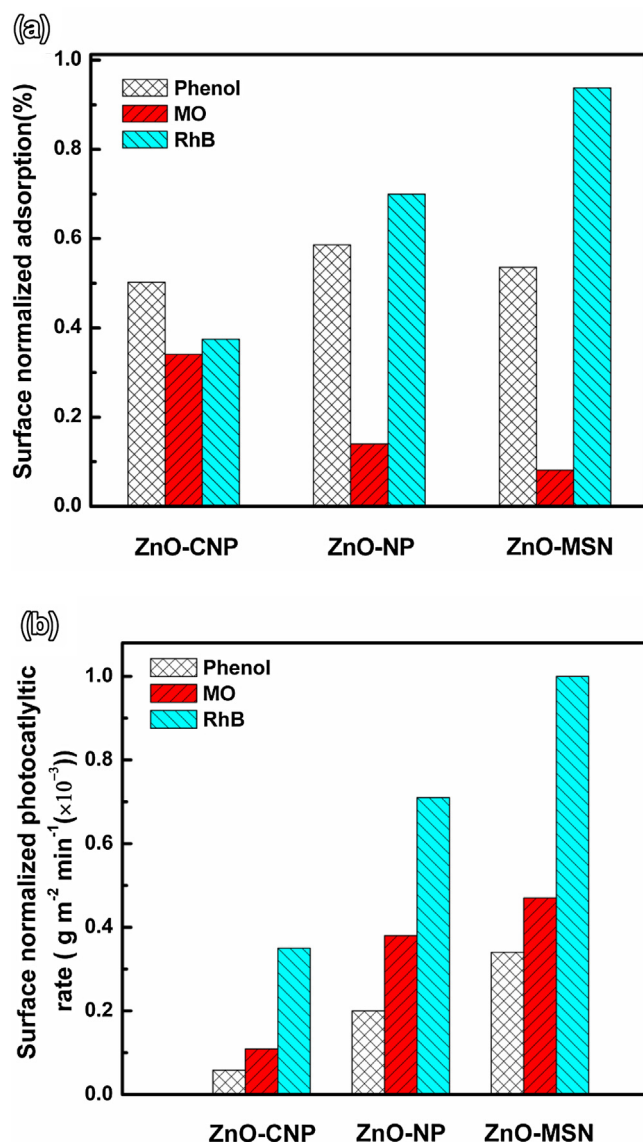


Fig. 6. (a) Surface normalized adsorption and (b) surface normalized photocatalytic rates of ZnO-MSN, ZnO-CNP and ZnO-NP towards the mixed molecules.

towards neutral phenol. However, both the ZnO-MSN and ZnO-NP show significantly selective adsorption towards anionic MO. Particularly, the ZnO-MSN demonstrates a much less adsorption capability towards MO, almost 4 times lower than that of ZnO-NP, indicating high repulsion to anionic MO. Further, the ZnO-MSN displays almost three times adsorption capability towards cationic RhB compared to the ZnO-NP. This implies that the ZnO-MSN presents highly selective adsorption toward positively charged RhB and almost no adsorption toward negatively charged MO compared to ZnO-NP. This high contrast toward positively charged RhB and negatively charged MO also indicates that the ZnO-MSN contains more negative charged O-terminated (000-1) surfaces, leading to more coulombic attraction with positively charged RhB and coulombic repulsion with negatively charged MO. To make sure of more negatively charged O-terminated (000-1) surfaces in the porous ZnO-MSN, the zeta potential measurement was carried out. Table 1 shows the values of the three samples. The value of ZnO-CNP is 15, which is three times to those of ZnO-MSN and ZnO-NP. This indicates that more negatively charged O-terminated (000-1) surfaces in the porous ZnO-MSN. It is interesting to note that the



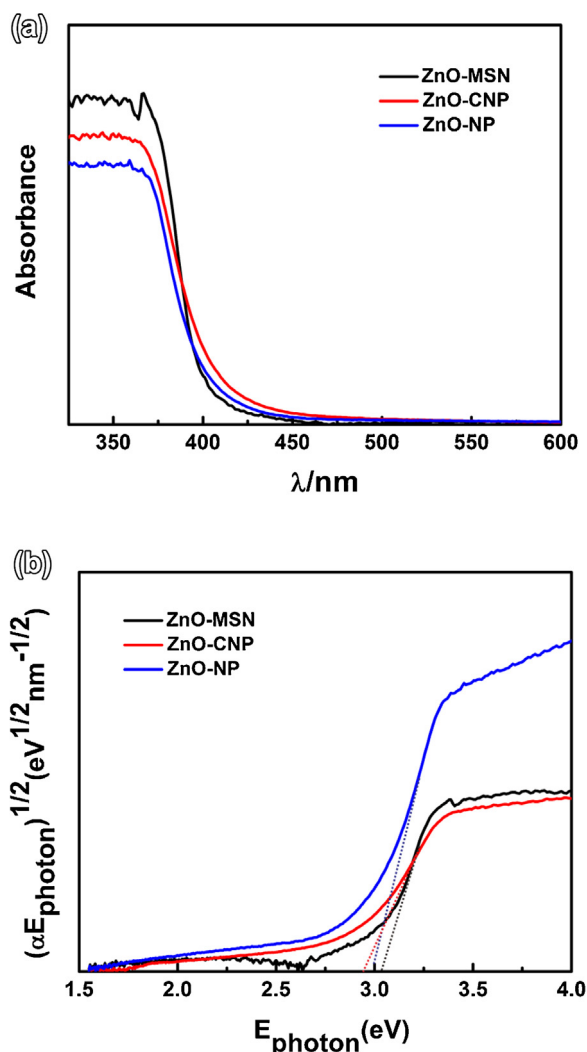


Fig. 7. (a) UV-vis absorption spectra and (b) plots of  $(\alpha E_{\text{photon}})^{1/2}$  versus  $E_{\text{photon}}$  used for the band gap of ZnO-MSN, ZnO-CNP and ZnO-NP.

zeta potential of ZnO-NP is very close to ZnO-MSN. This means that the ZnO-NP also has more negatively charged O-terminated (000-1) surfaces. It is reasonable because both the ZnO-MSN and ZnO-NP are prepared from EG-capped ZnO nanoparticles.

Fig. 6b presents the normalized photocatalytic rates of ZnO-MSN, ZnO-CNP and ZnO-NP for the mixed pollutant molecules. It displays that all the samples demonstrate similar activity trend for the three pollutant molecules. Both the ZnO-MSN and ZnO-NP demonstrate much higher photocatalytic rates than the ZnO-CNP due to the more negatively charged O-terminated (000-1) surfaces. The ZnO-MSN displays the highest photocatalytic rates. To elucidate the optical absorption property, UV-vis spectrophotometry is then used to reveal the energy structures and the optical absorption properties of the three samples (Fig. 7a), indicating the energy structures and the optical absorption for ZnO-MSN, ZnO-NP and ZnO-CNP are very close. The band gap energy is estimated according to Kubelka-Munk transformation via the intersect point between the tangent line of the steep curve and the wavelength axis [35]. The calculated band gap energy values of ZnO-MSN and ZnO-NP are 3.02 eV and 3.0 eV, respectively. However, the band gap of ZnO-CNP is a little shift to 2.94 eV (Table 1). This expanded absorbing of ZnO-CNP may be resulted by its preparation method. The UV-vis result of the three samples means that the difference among the three ZnO samples is not mainly from the band gap but mainly from their structures. Therefore, the high preferential adsorption selectivity and extraordinary performance of ZnO-MSN in photodegradation of organic molecules are closely related to its special structure. The more O-termination (000-1) surfaces among the {0001} polar facets have high chemical reactivity, leading to a significant photocatalytic activity enhancement. On the other hand, the single-crystal structure of ZnO-MSN provides direct electrical pathways for photogenerated charges smoothly walking through the nanosheet to accelerate the generated electron-holes separation and the electron transport [36], resulting the best photocatalytic rate. In addition, the mesoporosity of ZnO-MSN is beneficial for molecules diffusion to the catalyst surface. Therefore, the synergy of the mesoporosity, the exposed {0001} polar facets and the single crystal nature makes ZnO-MSN display the highest photocatalytic rate for RhB as schematic illustrated in Fig. 8.

#### 4. Conclusion

2D ZnO mesoporous single-crystal nanosheet has been successfully synthesized via an intriguing colloidal templating approach. The EG cation on ZnO nanoparticles surface is helpful for the nanosheet formation and the polymer colloids play dual roles on mesoporous generation and {0001} polar facets exposed to exterior. Such unique ZnO-MSN with single-crystal nature and {0001} polar facets in the porous structure shows a highly preferential

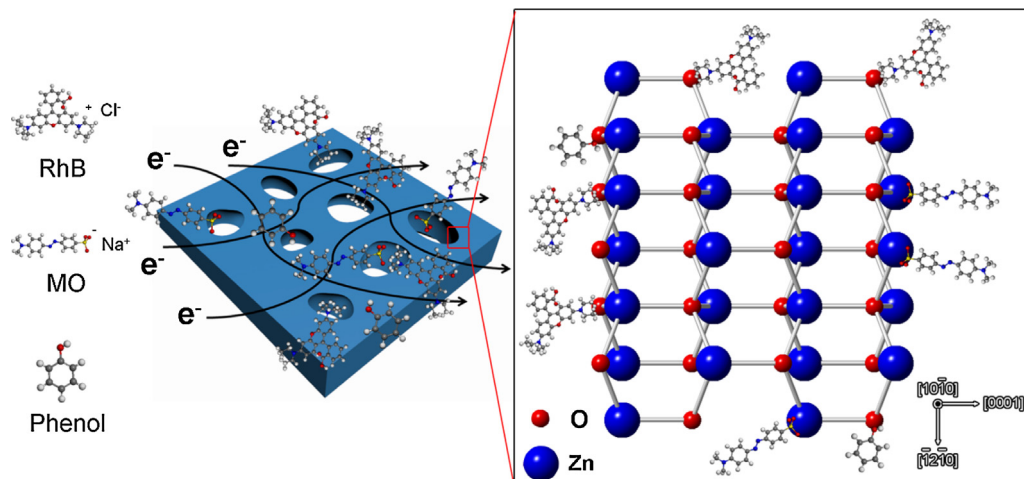


Fig. 8. The mechanism illustration of the photocatalytic decomposition of different charged organic molecules on ZnO-MSN.

selectivity and a significantly higher photodegradation rate for cationic RhB due to the single-crystal nature, porous structure and more exposed {000-1} polar facets with O-termination comparing to ZnO-CNP. The single-crystal nature results in better photocatalytic activity of ZnO-MSN than that of ZnO-NP. The ZnO-MSN with exposed {0001} polar facets is expected to be useful for other applications such as solar cells, photocatalytic water-splitting and gas sensing. Particularly, our synthesis strategy provides a feasible demonstration for synthesis of porous metal oxides single-crystal nanosheet with exposed polar surfaces.

## Acknowledgements

This work is realized in the frame of a program for Changjiang Scholars and Innovative Research Team (IRT1169) of Chinese Ministry of Education. B. L. Su acknowledges the Chinese Central Government for an “Expert of the State” position in the Program of the “Thousand Talents”. Y. Li acknowledges Hubei Provincial Department of Education for the “Chutian Scholar” program. This work is also financially supported by the Ph.D. Programs Foundation of Ministry of Education of China (20120143120019), Hubei Provincial Natural Science Foundation (2014CFB160) and the Fundamental Research Funds for the Central Universities (2013-YB-024). Z.Y. Hu, X.X. Ke and G. Van Tendeloo acknowledge the ERC Grant No. 246791-COUNTATOMS.

## Appendix A. Supplementary data

Supplementary data associated with this article can be found, in the online version, at <http://dx.doi.org/10.1016/j.apcatb.2015.07.054>

## References

- [1] Z.L. Wang, *J. Phys.: Condens. Matter* 16 (2004) 829.
- [2] J.Q. Hu, Y. Bando, J.H. Zhan, Y.B. Li, T. Sekiguchi, *Appl. Phys. Lett.* 88 (2003) 4414.
- [3] X.Y. Kong, Z.L. Wang, *Nano Lett.* 3 (2003) 1625.
- [4] E. Hosono, S. Fujihara, I. Honma, H. Zhou, *Adv. Mater.* 17 (2005) 2091.
- [5] D. Li, H. Haneda, *Chemosphere* 51 (2003) 129.
- [6] E.S. Jang, J.H. Won, S.J. Hwang, J.H. Choy, *Adv. Mater.* 18 (2006) 3309.
- [7] G.R. Li, T. Hu, G.L. Pan, T.Y. Yan, X.P. Gao, H.Y. Zhu, *J. Phys. Chem. C* 112 (2008) 11859.
- [8] A. McLaren, V.S. Teresa, G. Li, S.C. Tsang, *J. Am. Chem. Soc.* 131 (2009) 12540.
- [9] T.B. Hur, Y.H. Hwang, H.K. Kim, H.L. Park, *J. Appl. Phys.* 96 (2004) 1740.
- [10] Y. Zhang, M. Zhang, Y. Zhou, J. Zhao, S. Fang, F. Li, *J. Mater. Chem. A* 2 (2014) 13129.
- [11] X. Deng, K. Yao, K. Sun, W.X. Li, J. Lee, C. Matranga, *J. Phys. Chem. C* 117 (2013) 11211.
- [12] K. Lee, M. Kim, H. Kim, *J. Mater. Chem.* 20 (2010) 3791.
- [13] S. Liu, J. Yu, M. Jaroniec, *Chem. Mater.* 23 (2011) 4085.
- [14] C. Tusche, H. Meyerheim, J. Kirschner, *Phys. Rev. Lett.* 99 (2007), 26102-1.
- [15] X. Wang, Z. Tian, T. Yu, H. Tian, J. Zhang, S. Yuan, X. Zhang, Z. Li, Z. Zou, *Nanotechnology* 21 (2010) 0657031.
- [16] B. Li, Y. Wang, *J. Phys. Chem. C* 114 (2010) 890.
- [17] J. Zhang, S. Wang, M. Xu, Y. Wang, B. Zhu, S. Zhang, W. Huang, S. Wu, *Cryst. Growth Des.* 9 (2009) 3532.
- [18] Z.H. Jing, J.H. Zhan, *Adv. Mater.* 20 (2008) 4547.
- [19] L. Wang, Y. Zheng, X. Li, W. Dong, C. Li, X. Li, T. Zhang, W. Xu, *Thin Solid Films* 519 (2011) 5673.
- [20] X.L. Zhang, R. Qiao, R. Qiu, J.C. Kim, Y.S. Kang, *Cryst. Growth Des.* 9 (2009) 2906.
- [21] J. Zhang, H. Liu, Z. Wang, N. Ming, Z. Li, A.S. Biris, *Adv. Funct. Mater.* 17 (2007) 3897.
- [22] E.J. Crossland, N. Noel, V. Sivaram, T. Leijtens, J.A. Alexander Webber, H.J. Snaith, *Nature* 495 (2013) 215.
- [23] J. Liu, J. Jin, Y. Li, H.W. Huang, C. Wang, M. Wu, L.H. Chen, B.L. Su, *J. Mater. Chem. A* 2 (2014) 5051.
- [24] J. Jin, S.Z. Huang, J. Liu, Y. Li, D.S. Chen, H.E. Wang, Y. Yu, L.H. Chen, B.L. Su, *J. Mater. Chem. A* 2 (2014) 9699.
- [25] Y. Li, F. Piret, T. Leonard, B.L. Su, *J. Colloid Interface Sci.* 348 (2010) 43.
- [26] M. Wu, Y. Li, Z. Deng, B.L. Su, *ChemSusChem* 4 (2011) 1481.
- [27] M. Wu, J. Liu, J. Jin, C. Wang, S. Huang, Z. Deng, Y. Li, B.L. Su, *Appl. Catal. B: Environ.* 150–151 (2014) 411.
- [28] M. Wu, J. Jin, J. Liu, Z. Deng, Y. Li, O. Deparis, B.L. Su, *J. Mater. Chem. A* 1 (2013) 15491.
- [29] A. Wander, F. Schedin, P. Steadman, A. Norris, R. McGrath, T. Turner, G. Thornton, N. Harrison, *Phys. Rev. Lett.* 86 (2001) 3811.
- [30] O. Dulub, U. Diebold, G. Kresse, *Phys. Rev. Lett.* 90 (2003) 0161021.
- [31] V. Staemmler, K. Fink, B. Meyer, D. Marx, M. Kunat, S. Gil Girol, U. Burghaus, C. Wöll, *Phys. Rev. Lett.* 90 (2003) 1061021.
- [32] X.Y. Kong, Y. Ding, R.S. Yang, Z. Wang, *Science* 303 (2004) 1348.
- [33] D.V. Dyck, *J. Microsc.* 119 (1980) 141.
- [34] D.S. Chen, W.B. Yu, Z. Deng, J. Liu, J. Jin, Y. Li, M. Wu, L.H. Chen, B.L. Su, *RSC Adv.* 5 (2015) 55520.
- [35] M. Wu, A. Zheng, F. Deng, B.L. Su, *Appl. Catal. B: Environ.* 138–139 (2013) 219.
- [36] W.A. Tisdale, K.J. Williams, B.A. Timp, D.J. Norris, E.S. Aydil, X.Y. Zhu, *Science* 328 (2010) 1543.